Probing the density dependence of the quantum molecular dynamics potential with spallation neutrons induced by 1.2 GeV protons on Al, Fe, Zr, and Pb

Khaled Abdel-Waged*

Umm Al-Qura University, Faculty of Applied Science, Physics Department, Makkah Unit 126, P.O. Box 7047, Saudi Arabia

(Received 24 October 2005; revised manuscript received 30 May 2006; published 1 September 2006)

The dependence of spallation neutron production double-differential cross sections on the density of the quantum molecular dynamics potential is investigated in p+Al, Fe, Zr, and Pb reactions at 1.2 GeV. It is shown that the cascade component of the neutron spectra is largely unaffected by the parameters of the density-dependent potential. As for the evaporative part (<20 MeV), some differences are marked only for Pb. Calculated results with a Skyrme-type equation of state of $K = 300$ MeV reproduce the neutron spectra for the reactions under study.

DOI: 10.1103/PhysRevC.74.034601 PACS number(s): 25.40.Sc, 24.10.Lx, 25.40.Ep, 24.10.Pa

I. INTRODUCTION

Recently, several laboratories have made an extended effort to measure neutron spallation data induced by intermediate-energy (≈1 GeV) proton-nucleus interaction [1–4] in order to establish a base for the testing and validation of spallation microscopic transport models [5–12]. These data are also important in several areas, e.g., accelerator shielding, transmutation of transuranic wastes by spallation reactions, and medical applications.

Two major microscopic approaches are frequently applied: the intranuclear cascade (INC) models [5,6], in which the nuclear reactions are assumed to proceed from a succession of nucleon-nucleon (NN) collisions, and the quantum molecular dynamics (QMD) models [7–12], which account for both the multiple NN-scattering picture and the features of the mean field dynamics [or nuclear matter equation of state (EOS) effects].

As demonstrated in Refs. [5,11], the usage of realistic initial ground state configuration is essential in the INC and QMD models for the high predictive ability of the intermediate-energy (≈1 GeV) (p, nx) reactions. For QMD models [7, 8,11–13], optimum mean field parameters are required that allow realistic initial density/momentum distributions as well as long-time stability up to ≈100 fm/c and reasonable binding energy within ±0.5 MeV to a prediction of the liquid drop model. It was shown, within the Peilert QMD model [13], that adoption of the mean field of incompressibility $K = 380$ MeV seems to be useful in reproducing the high-energy part of the neutron spectra for p+Al, Zr, and Pb at incident energies between 80 and 800 MeV. The recent QMD calculations of Ref. [8] have demonstrated that the neutron spectra data for p + Pb at 590, 800, and 1500 MeV are described using a hard Skyrme-type EOS of $K \approx 380$ MeV. On the other hand, analysis with the JAERI QMD (JQMD) model [7] suggested that a soft Skyrme-type EOS (of $K = 237$ MeV) is more appropriate for reproducing the lower part of the neutron energy spectra for p+Fe and Pb from 113 MeV to 3 GeV. Thus these works do not provide the same conclusion for the EOS stiffness of that should be used to describe spallation neutrons. In other words, the mean field effects on spallation neutrons at intermediate energy in proton-induced reactions have not yet been seriously investigated.

In the present work, we study the effect of the density dependence of the QMD potential (mean field) which can be characterized by the nuclear incompressibility and EOS, on the recent data of the neutron energy-angle double-differential cross sections [4], in the framework of the ultra-relativistic QMD (UrQMD) model [14]. The UrQMD is designed to cover the best possibilities of the INC and QMD models in the energy range from BNL Alternating Gradient Synchrotron (AGS) energies ($E_{\rm lab} = 1$–$10A$ GeV) up to the full CERN Super Proton Synchrotron (SPS) energy ($E_{\rm lab} = 160A$ GeV). At AGS energies, these advantages include (i) all baryonic resonances up to an invariant mass of 2 GeV as well as mesonic resonances up to 1.9 GeV as tabulated by the Particle Data Group [15], (ii) self-consistent mean field dynamics, and (iii) medium modified angular distribution for NN elastic scattering. However, for a comprehensive description of spallation neutron data, several ingredients should be introduced in the standard UrQMD model [14]. The improved version, referred to as ImUrQMD and described in detail in Refs. [9–12], includes (i) a more realistic initial ground state, (ii) a momentum-dependent Pauli potential, (iii) medium modified angular distributions for quasi-inelastic NN scattering and the reverse, $N\Delta \rightarrow NN$ reaction, and (iv) a clusterization procedure, which is supplemented by the statistical multifragmenation decay (SMD) model for the description of slow evaporated neutrons.

The paper is organized as follows. Section II defines the basic ingredients of the ImUrQMD model. In Sec. III, ImUrQMD model predictions, coupled with different density-dependent interaction potential parameter sets, which can be characterized by the nuclear incompressibility, are compared with one another and with the recent measurements of neutron energy-angle double-differential cross sections induced by 1.2 GeV protons on Al, Fe, Zr, and Pb targets. We summarize and conclude this work in Sec. IV.

*Permanent address: Physics Department, Faculty of Science, Benha University, Benha, Egypt. Electronic address: khelwagd@yahoo.com

II. DESCRIPTION OF THE ImUrQMD MODEL

Our calculations are based on the ImUrQMD model described in Refs. [11,12]. We will drop the detailed description of the model, concentrating here only on those points which are important for understanding the calculation discussed in Sec. III.

Nuclear collisions are assumed to be described by the sum of independent binary hadron-hadron (hh) collisions. Each hh collision is assumed to take place at the distance of closest approach; that is, two particles collide if their distance d_{trans} fulfills the relation

$$d_{\text{trans}} \leqslant \sqrt{\frac{\sigma_{\text{tot}}}{\pi}}, \quad \sigma_{\text{tot}} = \sigma(\sqrt{s}, \text{type}). \tag{1}$$

The total cross section σ_{tot} depends on the center-of-mass (c.m.) energy ($\sqrt{s}$) and on the species and quantum number of the incoming particles; d_{trans} is defined as the covariant relative distance between the two particles:

$$d_{\text{trans}} = \sqrt{(\vec{r}_1 - \vec{r}_2)^2 - \frac{(\vec{r}_1 - \vec{r}_2)\cdot(\vec{p}_1 - \vec{p}_2)}{(\vec{p}_1 - \vec{p}_2)^2}}, \tag{2}$$

with $\vec{r}_i$ being the location and $\vec{p}_i$ the momentum in the rest frame of the colliding particles. The constraint of using the local rest frame of the colliding particles ensures that the cross section of the two particles is calculated in the same fashion and does not depend on the reference frame. The time order of the individual binary collisions, however, strongly varies with the respective reference frame [14]. In Ref. [14], the computational frame dependence was studied in the system S+S at 200 GeV/A. It was found that the particle multiplicities and collision numbers for this reaction vary by less than 3% between the laboratory frame and the c.m. frame.

The inelastic hh collisions produce resonances at low and intermediate energies, while at high energies ($\sqrt{s} = 5$ GeV for baryon-baryon and 3 GeV for meson-baryon and meson-meson reactions), color strings are formed and they decay into hadrons according to the Lund string model [16]. There are 55 baryon and 32 meson states as discrete degrees of freedom in the model as well as their antiparticles and explicit isospin projected states with masses up to 2.25 GeV/c^2. All of these hadronic states can propagate and reinteract in phase space.

The UrQMD uses a table look-up for the total and elastic proton-proton and proton-neutron cross sections. The details of other hh cross sections implemented in the UrQMD model can be found in [14].

In contrast to other microscopic transport models [5,7], the ImUrQMD model includes the medium modified angular distributions for the $NN \to NN$ and $NN \to N\Delta$ processes as well as changes to the Δ-mass distribution. It was shown in Ref. [10] that the quasi-inelastic and elastic peaks of the neutrons induced by 1.2 GeV protons on targets with $27 \leqslant A \leqslant 232$ can be only successfully described if the in-medium modified angular distributions are taken into account, while free parametrizations fail.

On the basis of QMD, mean field is enforced for the scattered nucleons. The interaction potential is

$$V = V_{\text{Skyrme}} + V_{\text{Symmetry}} + V_{\text{Yukawa}} + V_{\text{Coulomb}} + V_{\text{Pauli}}. \tag{3}$$

The Skyrme-type density-dependent interaction V_{Skyrme}, the density-dependent symmetry potential V_{Symmetry}, the Yukawa potential V_{Yukawa}, the Coulomb potential between protons V_{Coulomb}, and the Pauli potential V_{Pauli} are given by

$$\begin{aligned}
V_{\text{Skyrme}} &= \frac{t_1}{2\rho_0}\sum_{i=1}^{A}\sum_{\substack{k=1\\k\neq i}}^{A}\tilde{\rho}_{ik} + \frac{t_\gamma}{(\gamma+1)\rho_0^\gamma}\sum_{i=1}^{A}\left(\sum_{\substack{k=1\\k\neq i}}^{A}\tilde{\rho}_{ik}\right)^\gamma,\\
V_{\text{Symmetry}} &= \frac{c_s}{2\rho_0}\sum_{i=1}^{A}\sum_{\substack{k=1\\k\neq i}}^{A}\xi_i\xi_k\tilde{\rho}_{ik},\\
V_{\text{Yukawa}} &= \frac{V_0^{\text{Yuk}}}{2}\sum_{i=1}^{A}\sum_{\substack{k=1\\k\neq i}}^{A}\frac{1}{2\vec{r}_{ik}}\exp\left(\frac{1}{4\alpha\gamma_Y^2}\right)\\
&\quad\times\left\{e^{-\vec{r}_{ik}/\gamma_Y}\left[1-\text{erf}\left(\frac{1}{2\gamma_Y\sqrt{\alpha}}-\sqrt{\alpha}\vec{r}_{ik}\right)\right]\right.\\
&\quad\left.-e^{\vec{r}_{ik}/\gamma_Y}.\left[1-\text{erf}\left(\frac{1}{2\gamma_Y\sqrt{\alpha}}+\sqrt{\alpha}\vec{r}_{ik}\right)\right]\right\},\\
V_{\text{Coulomb}} &= \frac{1}{2}e^2\sum_{i=1}^{A}\sum_{\substack{j=1\\j\neq i}}^{A}\frac{1}{r_{ij}}\text{erf}(\sqrt{\alpha}r_{ij}),\\
V_{\text{Pauli}} &= \frac{1}{2}V_0^P\left(\frac{\hbar}{p_0q_0}\right)^3\left(1+\frac{1}{2\alpha q_0^2}\right)^{-3/2}\\
&\quad\times\sum_{i=1}^{A}\sum_{\substack{j=1\\j\neq i}}^{A}\exp\left(\frac{-\alpha r_{ik}^2}{2\alpha q_0^2+1}-\frac{p_{ik}^2}{2p_0^2}\right)\delta_{\tau_i\tau_k}\delta_{\xi_i\xi_k},
\end{aligned} \tag{4}$$

where $\vec{r}_{ik} = \vec{R}_i - \vec{R}_k$, $\vec{p}_{ik} = \vec{P}_i - \vec{P}_k$, τ_i and ξ_i denote the spin-isospin index of nucleon (i), and the interaction density $\tilde{\rho}_{ik} = (\alpha/\pi)^{3/2}e^{-\alpha(\vec{R}_i-\vec{R}_k)^2}$ with $\alpha = 0.25\ \text{fm}^{-2}$. Here ξ_i is 1 for protons and -1 for neutrons. The summation runs over all projectile and target nucleons, $\rho_0 = 0.168\ \text{fm}^{-3}$ is the normal nuclear density, and erf denotes the error function.

To study the effect of the density-dependent interactions on the spallation neutrons by means of the ImUrQMD model, the parameters t_1, t_γ, γ, V_0^{Yuk}, γ_Y, V_0^{Paul}, q_0, and p_0 should be adjusted to yield reasonable values for the binding energy, saturation density, and incompressibility of infinite nuclear matter. We found that the parameter sets listed in Table I meet these requirements. The parameter set 1 (without Pauli potential) is the default UrQMD parameters [14]. The parameter sets used in this work are fixed by keeping the original QMD parameters and adjusting the parameters of the Pauli potential to give good agreement with the systematic trend of binding energies of finite nuclei. It should be noted that the same set of Pauli potential parameters can also reproduce the properties of the Fermi gas at zero temperature and at various densities [17]. The density-dependent parameters of sets 2 and 3 are taken from Refs. [18,19].

For the present study, we used two kinds of EOSs, namely, soft ($K = 200$ MeV) and hard ($K = 300$ MeV) Skyrme-type EOSs. Note, however, that the EOS (and its incompressibility modulus) is also affected by several factors such as clusterization at subsaturation, effective mass, surface,

TABLE I. Parameters of the interaction potential.

Set	α (fm^{-2})	t_1 (MeV)	t_γ (MeV)	γ	c_s (MeV)	$V_0^{\rm Yuk}$ (MeV fm)	γ_Y (fm)	$V_0^{\rm Paul}$ (MeV)	q_0 (fm)	p_0 (MeV/c)	K (MeV)
1	0.25	−163.0	125.95	1.676	–	−0.498	1.4	30	5.64	400	300
2	0.25	−356.0	303.00	7/6	–	−0.498	1.4	30	5.64	400	200
3	0.25	−310.0	258.0	7/6	–	−0.498	1.4	30	5.64	400	200
4	0.25	−163.0	125.95	1.676	25	−0.498	1.4	30	5.64	400	300

symmetry, and the Pauli, Coulomb, and Yukawa potentials [20–22].

In our method, we do not define the ground state of nuclei as an energy minimum state of the system; while in a usual method, one gets the initial distribution by tuning the parameters of the forces (3) and searching the energy minimum state with the frictional cooling method [23]. The reason for this is that we would like to keep the (frequently applied) parameter sets for a better comparison with similar works [7,8,11,12]. The ground state of the nucleus is generated by packing $\overrightarrow{R_i}$ and $\overrightarrow{P_i}$ randomly based on the Woods-Saxon type distribution in the coordinate space and local Thomas-Fermi momentum based on the local density approximation. After the sampling, we make a preselection that is only the system for which the energy is equal to $E_0(A_0, Z_0) \pm 0.5A$ MeV, where $E_0(A_0, Z_0)$ is the ground state energy of a nonexcited nucleus of mass A_0 and charge Z_0 given by the liquid drop model. For the preselected system, we make a further test, i.e., we let the system evolve with time until 100 fm/c. Only the system for which the binding energy and root-mean-square radius maintain a smooth variation with time and without particle emission is finally selected.

In Fig. 1, we present the time evolution of binding energies $E_{\rm bind}$ and root-mean-square radii $r_{\rm r.m.s.}$ for ^{56}Fe and ^{208}Pb calculated by ImUrQMD with different parameter sets (with incompressibilities between 200 and 300 MeV). We present one selected event for each case. As one can see, the $E_{\rm bind}$ remain constant, whereas small fluctuations of $r_{\rm r.m.s.}$ are observed. For ^{56}Fe, the system undergoes small $r_{\rm r.m.s.}$ vibrations and is almost independent of EOS. On the contrary, for the ^{208}Pb case, an expansion mode is observed with sets 1 and 2 from $t = 20$ to 80 fm/c, where $r_{\rm r.m.s.}$ varies from 5.4 to 6.7 fm. The $r_{\rm r.m.s.}$ obtained with set 3 varies from 5.4 to 5.8 fm in the 20–80 fm/c interval, showing the best stability. It was also shown in [18] that QMD calculations with set 3 increase the time during which the ^{208}Pb nucleus is stable and in good shape to a period of about 3000 fm/c. At $t > 80$ fm/c, the system becomes stable for the three sets.

It should be noted that the $r_{\rm r.m.s.}$ obtained with sets 1 and 2 correspond to the results presented by other QMD models [7,24]. These fluctuations are very difficult to avoid because our initialization procedure does not guarantee that the nucleon density distribution corresponds to the exact minimum of the total energy.

Let us investigate whether the results of the final observables would depend on the expansion mode. This is shown later in Fig. 7, where we plot results of the multiplicity distributions of hot prefragments for p+Pb interactions calculated by ImUrQMD using sets 2 and 3. As one can see, the respective multiplicity distributions do not depend on the expansion mode. This has also been verified in Ref. [9], where we checked the dependence on the so-called expansion volume V_b

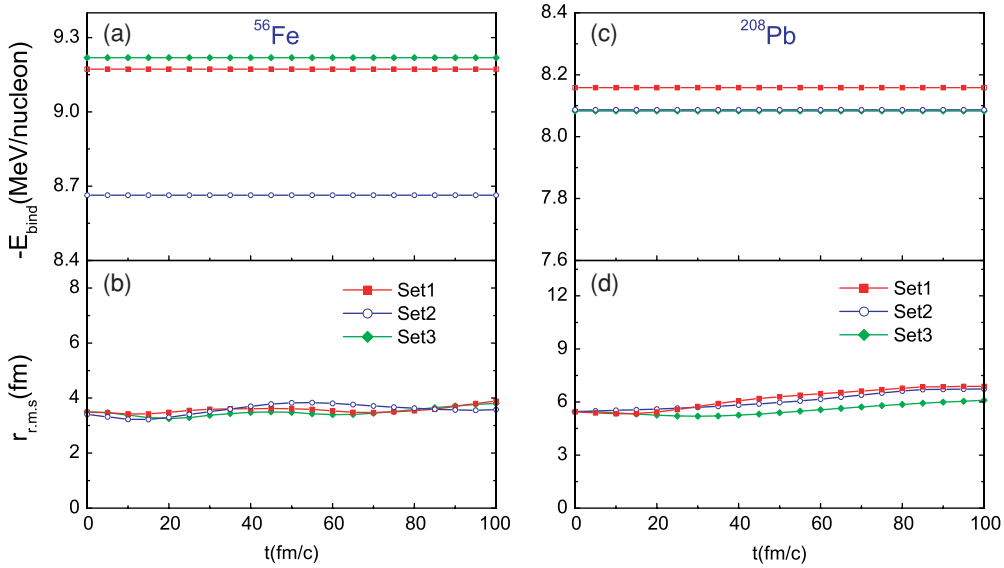

FIG. 1. (Color online) Time evolution of binding energy (a) and (c) and root mean square radius (b) and (d) of the ground state of Fe and Pb computed by ImUrQMD using three different parameter sets. The lines are the best fit to the results.

by stopping the UrQMD calculation at 100 fm/c and switching to the SMD model [25]. It was shown that the total neutron spectrum shape is not sensitive to the choice of V_b.

In Fig. 2, we show (a) the density distribution $\rho(r)$ and (b) the momentum distribution $g(p)$for the ground state of ^{56}Fe and ^{208}Pb nuclei calculated by ImUrQMD with different parameter sets. The results shown are quantities averaged over 100 events. The error bars in Fig. 2 denote the fluctuations in time evolution averaged over 100 events. The solid lines in Fig. 2(a) denote the empirical density distribution, while the ones in Fig. 2(b) are the empirical distribution parametrized by a superposition of two Gaussians [26]. We observe that for the ^{56}Fe system the calculations with different parameter sets produce equally good descriptions of the empirical distributions except for a rather wide tail in the case of set 2. As for the ^{208}Pb system, results with sets 1 and 3 are very similar and provide the best description of the density profiles, while set 2 leads to high density and low momentum at the center. The deviation in the results of set 2 from those of sets 1 and 3 is due to the higher (values of Skyrme parameters t_1 and t_γ, see Table I) attractive forces which push the nucleons into the center so that more nucleons will be in the high-density region. As shown in Fig. 2 (and later in Figs. 4 and 7), the effect of these forces becomes visible in the heaviest target system.

The common features of ImUrQMD calculations with different parameter sets are the diffuse nuclear surface and high momentum component. These features are shown in Refs. [11,12] to be essential for reproducing the neutron spectra for p+Al, Fe, and Zr reactions at 1.2 GeV. The latest JQMD calculations have corroborated our analysis and demonstrated that smaller density/momentum distributions

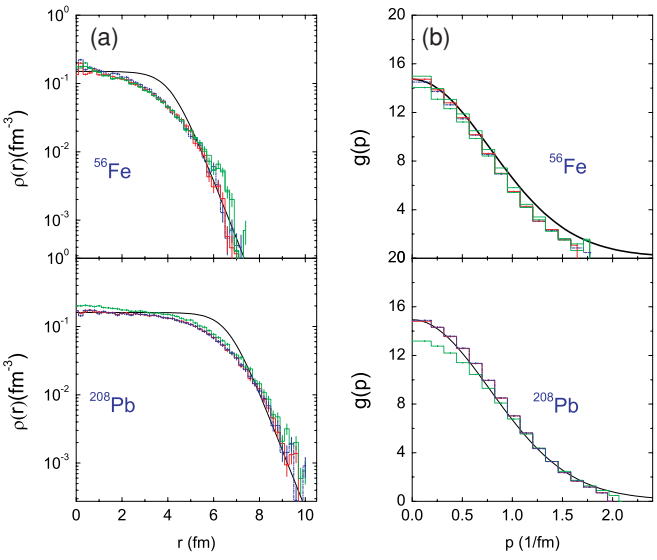

FIG. 2. (Color online) (a) Profile density distribution $\rho(r)$ and (b) momentum distribution $g(p)$of the ground state of Fe and Pb obtained by set 1 (solid red histograms), set 2 (short-dotted green histograms), and set 3 (dash-dotted blue histograms) averaged over 100 events. The smooth solid lines designate the empirical Woods-Saxon density (left panels) and the two Gaussian momentum distributions (right panels).

lead to inconsistencies in proton spectra for p+C, Al, and Nb reactions at 300 and 392 MeV [27].

From Figs. 1 and 2, one may conclude that there is a visible EOS difference in the time evolution and density/momentum distribution in light and heavy systems, but calculations with different Skyrme-type EOSs fulfill the static properties of the ground state of both systems.

It is worth mentioning that the density-dependent parameter sets presented in Table I have been employed in the literature [18,28–30]. For example, in Ref. [30] the excitation function of pion multiplicities in central Au+Au reactions from 0.4A to 1.5A GeV were compared within the UrQMD approach. A good agreement with the data has been found when using sets 1 and 2. In addition, by introducing set 3 in the QMD model of Ref. [18], the fusion excitation functions for a series of fusion reactions were calculated and the results were in good agreement with the experimental data.

The ImUrQMD calculation is carried out up to a time scale referred to as the transition time $t_{\rm tr}$. We have selected $t_{\rm tr}$ to be 100 fm/c, because this value was high enough to obtain stable neutron spectra from the (p, xn) reaction against a change of $t_{\rm tr}$ as shown in Ref. [9]. At $t_{\rm tr} = 100$ fm/c, the position of each nucleon is used to calculate the distribution of mass and charge numbers of clusters referred to as "prefragments." In determining the mass and charge numbers of the prefragments, the minimum spanning tree method [24] is employed, and a prefragment is formed if the centroid distances are lower than $R_{\rm clus}$. In this paper, $R_{\rm clus}$ is fixed at 4 fm. The prefragments thus identified are then Lorentz boosted into their rest frames to evaluate their excitation energies. The excitation energies $(\varepsilon)^*$ of the hot prefragments are calculated as the differences between the binding energies of the hot prefragments and the binding energies of these prefragments in their ground state. When the prefragment is in the excited state, the SMD model [25] is employed as an afterburner, which is shown to be better suited than the standard sequential evaporation model for descibing the slow evaporated neutrons [9].

III. RESULTS AND DISCUSSION

In this section, we display the predictions of the ImUrQMD model (coupled with different potential parameter sets) along with recent measurements [4] of energy-angle double-differential cross sections of neutrons induced by 1.2 GeV protons on Al, Fe, Zr, and Pb.

The experimental energy spectra (see Figs. 3 and 4) show at 0° two prominent peaks. These peaks are less pronounced at 10° and are insignificant at 25° and larger. The (quasielastic) peak, characterized by a narrow peak at a kinetic energy near that of the beam energy, is due to a single (p, n) elastic scattering in the forward direction. The (quasi-inelastic) peak, centered around 873 and 760 MeV at 0° and 10°, respectively, is about 400 MeV wide and is thought to be due to Δ-resonance excitation. In addition to these two peaks, it seems that two components exist for all of the spectra [7,9]: one is a shoulder below $E_n \approx 10$ MeV, the other is a wide peak extending up to a few hundred MeV. The low-energy neutrons mostly come from evaporation of the excited target residues through

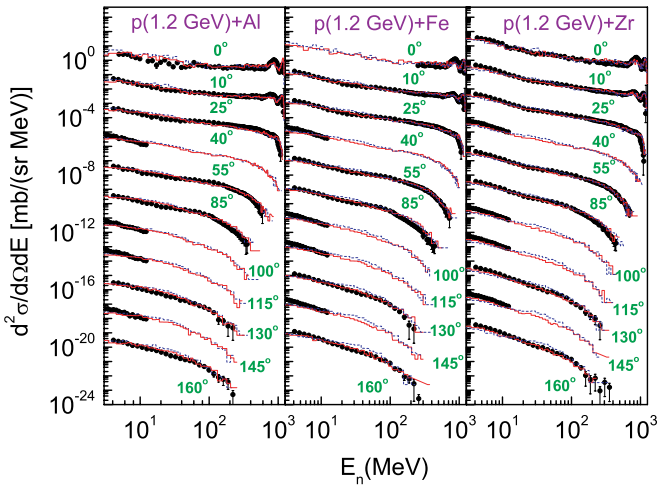

FIG. 3. (Color online) Neutron energy-angle double-differential cross sections for 1.2 GeV protons on Al, Fe, and Zr. Predictions by ImUrQMD using sets 1 and 3 are given by solid (red) and short-dashed (blue) histograms, respectively. Data (solid circles with error bars) are from [4]. For clarity, only the histograms and data for the smallest angles are given in absolute value. The others have been multiplied by 10^{-2}, 10^{-4}, . . . for other angles in increasing order.

the equilibration process. The other component becomes less pronounced with increasing angles. This component arises from (cascade) processes involving several NN collisions. We note that the three components exist for all spallation reactions induced by an intermediate energy ($\approx$1 GeV) proton on various targets [4]. Below, we are going to investigate the effect of the density-dependent potential (EOS effects) on the slow evaporated and cascade neutrons by employing the ImUrQMD model. We performed 30 000 simulations at various impact parameters from 0 to 3, 4, 5, and 7 fm for Al, Fe, Zr, and Pb, respectively, which were selected as slightly bigger than the corresponding nuclear radii. In order to have sufficient statistics, calculations were done for angular bins of $\pm$3.5 at 0° and $\pm$5 for larger angles.

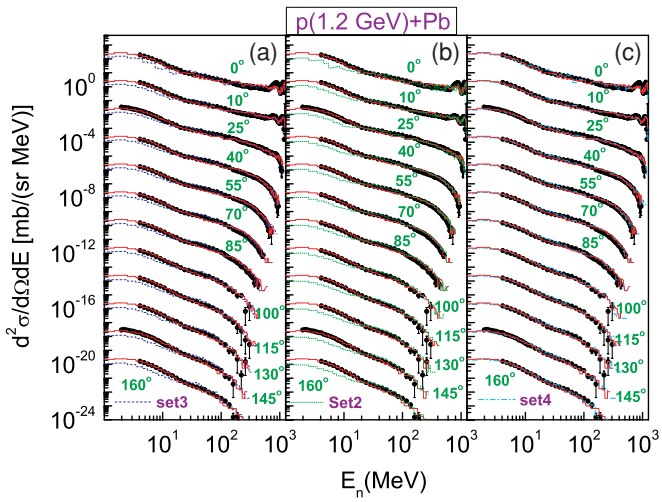

FIG. 4. (Color online) Same as Fig. 3, but for Pb target. Also shows results for (b) set 2 and (c) set 4.

The error bars in Figs. 3 and 4 include statistical uncertainty only [4]. Target thickness also induces some distortion in the neutron double-differential spectra, which results in a depopulation of the intermediate-energy part of the spectra (between 200 and 600 MeV) and a 20 MeV downward shift of the location of the quasielastic peak [4]. Calculations using the LAHET high-energy transport code system [31] were performed in Ref. [4] for targets with actual geometry and an infinitely thin one in order to assess the order of magnitude of the depopulation. It was shown that the difference is very small for the Pb target and becomes larger as both the target mass number and angle decrease.

In Fig. 3, we compare the ImUrQMD results with the experimental data for p+Al , Fe, and Zr reactions at 1.2 GeV. Calculations with sets 1 and 3 are selected here. Solid lines show the calculation results of ImUrQMD by using set 1; short-dashed lines, using set 3. As one can see, for p+Al and Fe interactions, the short-dashed lines enhance the slow evaporated neutrons at forward ($\theta < 25°$) and backward ($\theta > 100°$) angles in agreement with the data. However, for p+Zr interactions, the solid lines better reproduce the slow evaporated neutrons. As for the cascade neutrons, the short-dashed lines tend to be higher than the experimental data in the region of 17–50 MeV at $\theta < 85°$and in the region of 17–85 MeV at $\theta > 85°$ for the specified reactions. In contrast, solid lines more closely reproduce experimental data in these regions. In other words, adoption of hard Skyrme-type EOS (with $K = 300$ MeV) is mainly useful in reproducing cascade neutrons for p+Al, Fe, and Zr reactions at intermediate energy. The ImUrQMD calculations using set 2 (not shown here) yield similar results as those of set 3. This is expected since both sets produce the same initial density/momentum distributions and incompressibilities for the three interactions.

As shown in Fig. 4, the density-dependent effects become more pronounced when the target becomes heavier, especially in the low-energy region. Here, the short-dotted and dash-dotted lines denote the results using sets 2 and 4, respectively. Figure 4(a) shows that set 1 (solid lines) is highly successful in reproducing the evaporation part of the spectra at all angles. The cascade parts of the spectra are also well reproduced, except for a slight underestimation in the high-energy part ($\geqslant$100 MeV) at 160°. In contrast, the results of set 3 underestimate the slow evaporated neutrons, especially at the most forward and backward angles. Although at $>$85° there is a slight overestimation of cascade neutrons (between 20 and 100 MeV, roughly) and the tendency is similar to light (Al, Fe) and medium (Zr) targets, better accounts have been obtained. The results for set 2 appear to be similar to those for set 3 in the cascade region [see Fig. 4(b)]. A noticeable difference, however, exists for slow evaporated neutrons, where the results using set 2 tend to be lower than those of set 3 and the data [cf. Figs. 4(b) and 4(a)]. In Fig. 4(c), we study the effect of the density-dependent symmetry potential on the neutron spectra. The figure shows that the symmetry potential effect on the slow evaporated and cascade neutrons is small, but it improves the description of cascade neutrons in the region of 20 to 110 MeV.

Comparing Figs. 3 and 4, we see that the effect of the density-dependent potential on the cascade component

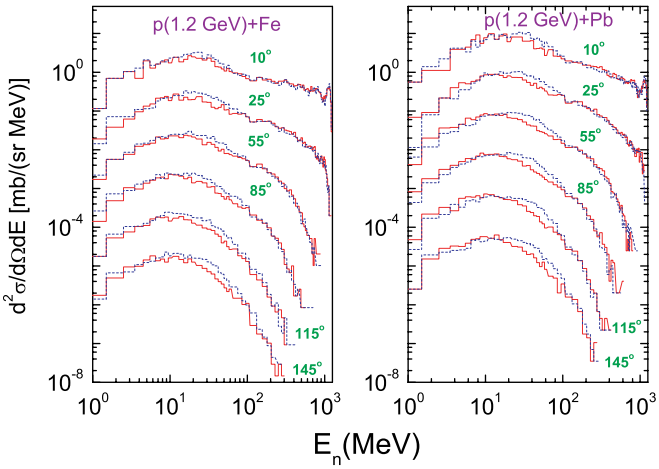

FIG. 5. (Color online) Low- and high-energy cascade neutrons as predicted by ImUrQMD (SDM is switched off) using set 1 (solid red histograms) and set 3 (short-dashed blue histograms) for the reactions p+Fe and p+Pb. Spectra are scaled by the factors 10^0, 10^{-1}, 10^{-2}, 10^{-3}, 10^{-4}, and 10^{-5} from top to bottom.

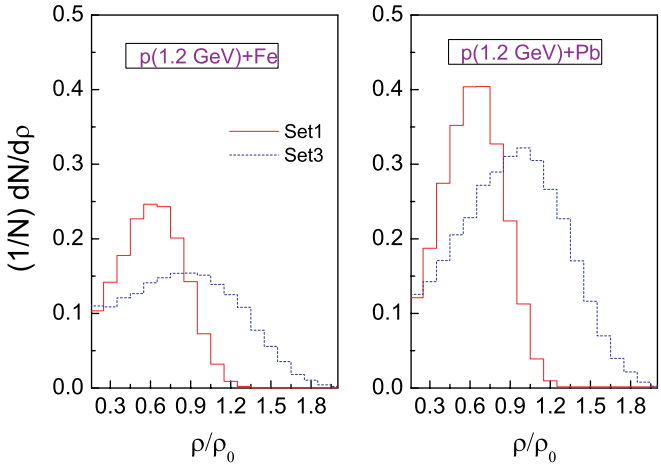

FIG. 6. (Color online) Normalized neutron multiplicities as a function of density at the space coordinates where the neutrons have been collided more than once. p+Fe and p+Pb reactions are considered, ImUrQMD calculations are performed with sets 1 and 3.

is relatively small for p+Al, Fe, and Zr reactions and is practically vanishing for Pb. As for the evaporative part, a visible EOS dependence of the spallation neutron spectra exists in p+Pb reactions.

Let us further investigate the density-dependent (EOS) effects on cascade neutrons. In Fig. 5, we display the ImUrQMD calculations without evaporation (SDM is switched off) using set 1 (solid lines) and set 3 (short-dashed lines) for p+Fe (left panel) and Pb (right panel) interactions at 1.2 GeV. We see that the influence of the density-dependent interaction depends on the nucleon energy, scattering angle, and mass number of the target nucleus. In particular, the low-energy (cascade) neutrons ($<$10 MeV) are more affected by the density-dependent potential in p+Pb reactions than in p+Fe reactions, where the stiff EOS leads to more low-energy (cascade) neutrons, compared to the soft one, especially at intermediate angles. At the higher energy side, however, the soft Skyrme-type EOS results in larger cascade neutrons, and the effect is seen to be more pronounced for both targets. This change of behavior from low- to high-energy regions is due to the increase of the number of NN collisions. We also note that the effect of the density-dependent interactions on the high-energy (cascade) neutrons is more pronounced for Fe than for Pb at backward angles ($\theta > 85^\circ$). This may imply that the effect becomes smaller as the number of collisions increases.

To obtain a quantitative picture of the explored density effects on cascade neutrons, the neutron densities are shown in Fig. 6 for free neutrons that have collided more than once. Free neutrons were selected using the requirement that the distance to the closest nucleon within a given ensemble is more than some critical distance $d_c = 4$ fm in order to separate them from neutrons bound in prefragments. Figure 6 illustrates several features. The density distributions are narrower in the case of the hard Skyrme-type EOS as compared to the soft one. Generally, densities above $1\rho_0$are rarely reached using set 1, whereas with set 3 the free neutrons are collided at densities up to $1.8\rho_0$. Comparing Figs. 5 and 6, we deduce that the low-energy (cascade) neutrons are more likely emitted at $\rho < 0.6\rho_0$ where the density-dependent interactions are stronger with the stiff EOS. In addition, the excess of cascade neutrons obtained with the soft Skyrme-type EOS originates almost exclusively from higher density $\rho > \rho_0$ matter, which demonstrates that the incident proton reaches the deep inside of the target nucleus and the number of NN collisions, thus, increases.

The systematic difference between the results obtained with sets 2 and 3 in the evaporation region can be interpreted as follows. In the case of set 2, nucleons in a prefragment are more bound because of the higher (values of Skyrme parameters t_1 and t_γ, see Table I) attractive forces. On the other hand, with set 3 the nucleons are less bound, and the prefragment becomes more excited, and the number of evaporated neutrons increases. This assumption can be verified in Fig. 7, where we investigate the influence of both sets on the multiplicity and excitation energy distributions of prefragments for p+Fe, Zr, and Pb interactions. We see that the respective multiplicity distributions are similar for the studied interactions, whereas the excitation energy distributions obtained with set 3 extend to higher values than those obtained with set 2 as the target becomes heavier. Next, we turn to the difference between the ImUrQMD predictions using soft (with sets 2 and 3) and hard (with set 1) Skyrme-type EOSs in the lower energy part of the neutron spectra for the reactions under study. We see that the distributions of light ($<A_0/6$) prefragments calculated with different EOSs are nearly the same, where A_0 is the mass number of the prefragment. On the other hand, lower emission of intermediate ($A_0/6 < A < 5A_0/6$) and large ($>0.96A_0$) prefragments is observed in the soft Skyrme-type EOS compared to the hard one as the target becomes heavier. This indicates that the intermediate and large prefragments produced using a hard Skyrme-type EOS are the main source of the copious production of slow evaporated neutrons, especially for p+Pb interactions. The observation of a greater number of intermediate mass fragments using

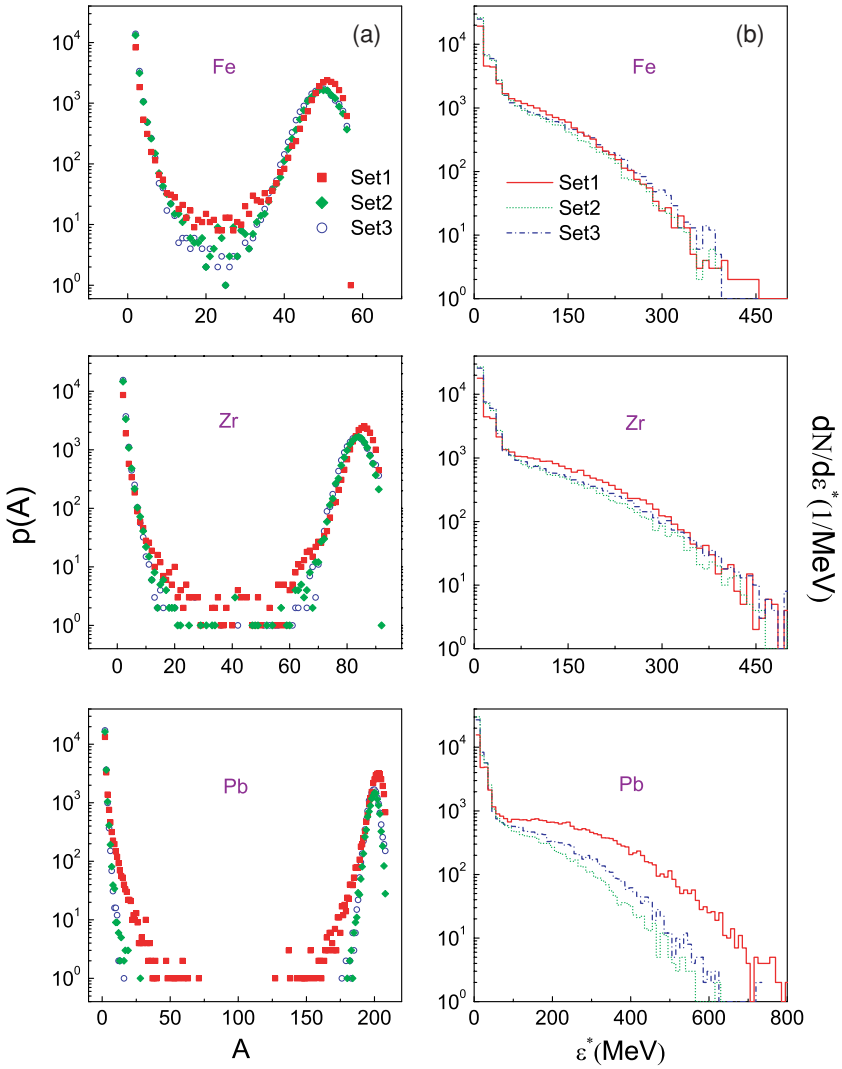

FIG. 7. (Color online) (a) Multiplicity distributions and (b) excitation energy distributions of prefragments in the p+Fe, Zr, and Pb interactions with different parameter sets.

the hard Skyrme-type EOS compared to the soft one is also consistent with results obtained in the study of Au (10.6A GeV)+emulsion interactions by a two-step model based on QMD [32].

Thus, one may conclude that the ImUrQMD calculations with hard Skyrme-type EOS ($K = 300$ MeV) provide the most reasonable description of the spallation neutron spectra for p+Al, Fe, Zr, and Pb interactions at 1.2 GeV. It should also be mentioned that the Cugnon INC model [5] seems to yield good results comparable to ours for the reactions under investigation at forward and backward angles, but they are less satisfactory at intermediate angles, pointing to a possible lack of mean field effects. With a set of potential parameters that corresponds to $K = 237$ MeV, the JQMD model gave overall agreements with the data. However, the high-energy part calculated by the JQMD model is often smaller than the data [7].

Finally, it is interesting to note that results of the relativistic Boltzmann-Uehling-Uhlenbeck model [33] (a hadronic cascade + JQMD model [34]) applying a common mean field of $K = 300$ (314) MeV reproduce the experimental data of proton sideward, directed, and elliptic flows in an incident energy range of 0.25A–11A(2A–158A) GeV. Also, $K = 250$ MeV [35] is found to be the lower bound for the nuclear matter incompressibility modulus in nuclear structure models based on the relativistic mean field approximation.

IV. SUMMARY AND CONCLUSIONS

The improved UrQMD (ImUrQMD) calculations have been performed for the energy-angle neutron double-differential cross sections induced by 1.2 GeV protons on Al, Fe, Zr, and Pb. To assess the effect of the density-dependent part of the QMD potential, we incorporated four different parameter sets (see Table I). We found that the effect changes as the mass number of the target increases (see Figs. 3 and 4). The cascade component (20–100 MeV) of the neutron spectra is slightly affected by the parameters of the mean field for p+Al, Fe, and Zr reactions. Concerning the p+Pb reactions, the mean field effect is practically vanishing. As for the evaporative

part (<20 MeV), a marked difference is only seen for p+Pb reactions. The data appear to suggest a hard Skyrme-type EOS of $K = 300$ MeV. The dependence on the Skyrme forces and symmetry energy was also studied. The former (latter) is defined as the difference between the ImUrQMD results employing set 3(1) and set 2(4); both sets have the same incompressibility. For the heaviest system, the Skyrme forces affect the evaporation region, while the symmetry energy leads to a slight enhancement of the neutron spectra in the region of 20 to 110 MeV, in agreement with the data.

Finally, it should be pointed out that there are still many problems to solve before pinning down the equation of state. First, one has to take advantage of all the data, i.e., neutron spectra at other energies, proton spectra, and mass residue spectra. Second, there are uncertainties linked with the particular choices of the quasiclassical UrQMD model ingredients, for example, the quality of the initial configuration, the hypothesis of free cross sections, and the neglect of an additional momentum-dependent potential. Third, it is necessary to test various mean field treatments such as the Lorentz scalar and nonrelativistic type density-dependent potential [36], the relativistic mean field having Lorentz scalar and vector terms [33], and constraint Hamiltonian dynamics [37].

ACKNOWLEDGMENTS

It is a pleasure to thank the UrQMD collaborators, in particular Dr. H. Weber, for making the URQMD code (version 1.2) available to us. We are grateful to Prof. S. Leray (Laboratoire National SATURNE) for providing us with the raw data presented here. We also wish to thank Dr. L. Qingfeng (Johann Wolfgang Goethe-Universitat), Prof. F. Sheng (China Institute of Atomic Energy), and Prof. J. Randrup (Lawrence Berkeley Laboratory) for private communications.

[1] L. Pienkowski, F. Goldenbaum, D. Hilscher, U. Jahnke, J. Galin, and B. Lott, Phys. Rev. C **56**, 1909 (1997).
[2] X. Ledoux *et al*., Phys. Rev. C **57**, 2375 (1998).
[3] K. Ishibashi *et al*., J. Nucl. Sci. Technol. **34**, 529 (1997).
[4] S. Leray *et al*., Phys. Rev. C **65**, 044621 (2002).
[5] A. Boudard, J. Cugnon, S. Leray, and C. Volant, Phys. Rev. C **66**, 044615 (2002).
[6] E. Suetomi, N. Kishida, and H. Kadotani, Phys. Lett. **B333**, 22 (1994).
[7] K. Niita, S. Chiba, T. Maruyama, T. Maruyama, H. Takada, T. Fukahori, Y. Nakahara, and A. Iwamoto, Phys. Rev. C **52**, 2620 (1995).
[8] F. Sheng, L. Zhuxia, Z. Zhixiang, and D. Dazhao, Eur. Phys. J. A **4**, 61 (1999); S. Fan, Z. Li, and Z. Zhao, Nucl. Sci. Eng. **142**, 195 (2002); S. Fan, J. Rong, H. Zhang, and Z. Zhao, *ibid*. **144**, 219 (2003).
[9] Kh. Abdel-Waged, Phys. Rev. C **67**, 064610 (2003).
[10] Kh. Abdel-Waged, Phys. Rev. C **70**, 014605 (2004).
[11] Kh. Abdel-Waged, Phys. Rev. C **71**, 044607 (2005).
[12] Kh. Abdel-Waged, J. Phys. G: Nucl. Part. Phys. **31**, 739 (2005).
[13] G. Peilert, J. Konopka, H. Stocker, W. Greiner, M. Blann, and M. G. Mustafa, Phys. Rev. C **46**, 1457 (1992).
[14] S. A. Bass *et al*., Prog. Part. Nucl. Phys. **41**, 225 (1998).
[15] R. M. Barnett *et al*. (Particle Data Group), Phys. Rev. D **54**, 1 (1996).
[16] B. Andersson, G. Gustafson, and B. Nilsson-Almqvist, Nucl. Phys. **B281**, 289 (1987).
[17] H. Liu and J.-Y. Liu, Z. Phys. A **354**, 311 (1996).
[18] J. Aichelin, Phys. Rep. **202**, 233 (1991).
[19] N. Wang, Z. Li, X. Wu, J. Tian, Y. X. Zhang, and M. Liu, Phys. Rev. C **69**, 034608 (2004).
[20] G. Peilert, J. Randrup, H. Stocker, and W. Greiner, Phys. Lett. **B260**, 271 (1991).
[21] A. Z. Mekjan, S. J. Lee, and L. Zamick, Phys. Rev. C **72**, 044305 (2005).
[22] C. Dorso and J. Randrup, Phys. Lett. **B215**, 611 (1988).
[23] D. H. Boal and J. N. Glosli, Phys. Rev. C **38**, 1870 (1988).
[24] Ch. Hartnack, R. K. Puri, J. Aichelin, J. Konopka, S. A. Bass, H. Stocker, and W. Greiner, Eur. Phys. J. A **1**, 151 (1998).
[25] J. B. Bondorf, A. S. Botvina, A. S. Iljinov, I. N. Mishustin, and K. Sneppen, Phys. Rep. **257**, 134 (1995).
[26] Y. Haneishi and T. Fujita, Phys. Rev. C **33**, 260 (1986).
[27] T. Kin *et al*., Phys. Rev. C **72**, 014606 (2005).
[28] Q. Li, Z. Li, E. Zhao, and R. K. Gupta, Phys. Rev. C **71**, 054907 (2005).
[29] Q. Li, Z. Li, S. Soff, M. Bleicher, and H. Stocker, Phys. Rev. C **72**, 034613 (2005).
[30] Q. Li, Z. Li, S. Soff, M. Bleicher, and H. Stoecker, J. Phys. G: Nucl. Part. Phys. **32**, 151 (2006).
[31] R. E. Parel and H. Liechtenstein, Report LA-UR-89-3014, Los Alamos National Laboratory, 1989 (unpublished).
[32] Kh. Abdel-Waged, J. Phys. G: Nucl. Part. Phys. **28**, 2951 (2002).
[33] P. K. Sahu, W. Cassing, U. Mosel, and A. Ohnishi, Nucl. Phys. **A672**, 376 (2000).
[34] M. Isse, A. Ohnishi, N. Otuka, P. K. Sahu, and Y. Nara, Phys. Rev. C **72**, 064908 (2005).
[35] D. Vretenar, T. Niksic, and P. Ring, Phys. Rev. C **68**, 024310 (2003).
[36] A. B. Larionov, W. Cassing, C. Greiner, and U. Mosel, Phys. Rev. C **62**, 064611 (2000).
[37] H. Sorge, H. Stocker, and W. Greiner, Ann. Phys. (NY) **192**, 266 (1989).